

Finite-Element Study of Motion-Induced Eddy Current Array Method for High-Speed Rail Defects Detection

Guanyu Piao^{ID 1}, Jiaoyang Li^{ID 1}, Lalita Udupa¹, *Life Fellow, IEEE*, Jianliang Qian^{ID 2}, and Yiming Deng^{ID 1}

¹Department of Electrical and Computer Engineering, Michigan State University, East Lansing, MI 48824 USA

²Department of Mathematics, Michigan State University, East Lansing, MI 48824 USA

Nondestructive testing (NDT) methods are widely used in the rail industry to detect and characterize rolling contact fatigue (RCF) defects in railroads, which is very important for railway inspection and maintenance to prevent catastrophic accidents. Existing NDT methods, e.g., ultrasonic testing (UT), magnetic flux leakage (MFL), and eddy current testing (ECT) have been successfully applied in the rail industry, and the state-of-the-art UT method reported recently achieved a high speed of 40 mi/h with a probability of detection (POD) over 80% under 30% false alarms. However, NDT methods still suffer from a bottleneck in that a higher inspection speed causes lower detection sensitivity due to their physical limits, such as negative velocity effect and long sensing time. One of the leading challenges to the rail NDT community is to develop a high-speed high-sensitivity (HSHS) capability that can provide an improved POD of rail defects in high-speed inspection scenarios over 60 mi/h. This article proposes a horizontal U-shaped magnets-based motion-induced eddy current array (MIECA) method to detect rail surface defects with the HSHS capability. The MIECA method deploys a three-axis magnetic sensor array along the rail transverse direction at the middle of the magnets to measure the MIECA signals, which utilizes the wake effect of the diffused motion-induced eddy current (MIEC) caused by the relative high-speed motion between the magnets and the rail track. Finite-element method (FEM) simulations with a wide speed range from 0 to 62.5 mi/h are carried out to investigate the relationships between the MIEC generation, diffusion and magnitude, and the three-axis MIECA signals. The simulation results show that the higher the speed, the greater the magnitude of diffused MIEC, and the greater the peak-to-peak values of three-axis MIECA signals caused by rail surface defects, which shows a great promise for detecting rail surface defects in high-speed scenarios and is superior inspection relative to existing NDT methods in terms of inspection speed, detection sensitivity, and defect characterization capability.

Index Terms—Finite-element method (FEM) simulations, high-speed rail inspection, motion-induced eddy current (MIEC), nondestructive testing (NDT), rolling contact fatigue (RCF).

I. INTRODUCTION

RAILWAY transportation is one of the most efficient modes for moving people and goods on the Earth's surface. Comparing to highway, marine, and air transportation, railway transportation has the advantages of large load capacity, high reliability, and efficiency, and environmental friendliness. For the global railway industry, train and railroad maintenance is an essential ingredient in the successful running of a railway [1]. Among them, railroad is the most vulnerable part because high contact stresses between train wheel and railroad are prone to induce rolling contact fatigue (RCF) damages on the rail head, which will gradually grow to become rail defects with accumulated traffic of mileage and tonnage [2]. Fig. 1 shows several typical rail defects at different rail regions, such as rail head, rail web, and rail base [3]. These rail defects will eventually form broken rails without proper inspection and maintenance that may lead to catastrophic railway accidents [4]. Thus, regular scheduled inspection and maintenance of railroad are very important to ensure railway safety.

It has been nearly a century since the nondestructive testing (NDT) methods were first used in the field test to

Manuscript received June 19, 2021; revised August 29, 2021; accepted October 5, 2021. Date of publication October 11, 2021; date of current version November 18, 2021. Corresponding author: Y. Deng (e-mail: dengyimi@msu.edu).

Color versions of one or more figures in this article are available at <https://doi.org/10.1109/TMAG.2021.3119267>.

Digital Object Identifier 10.1109/TMAG.2021.3119267

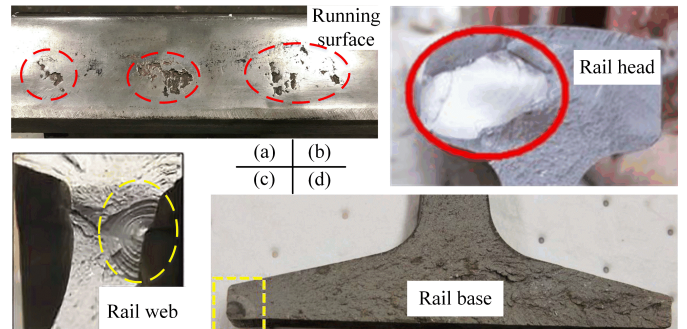


Fig. 1. Typical rail defects. (a) RCF defects on rail running surface. (b) Transverse fissure under shelling. (c) Rail web defect. (d) Rail base defect.

detect and characterize rail defects [5]. With the development of NDT, various methods have been studied and applied to railway inspection, including conventional ultrasonic testing (UT) [6], phased array UT (PAUT) [7], electromagnetic acoustic transducer (EMAT) [8], eddy current testing (ECT) [9], eddy current pulsed thermography (ECPT) [10], magnetic flux leakage (MFL) [11], alternative current field measurement (ACFM) [12], and electromagnetic field imaging (EMFI) [13]. Table I provides a summary of the main NDT methods applied in the rail industry in terms of highest inspection speed, defects detection capability, and deficiency. The ultrasonic wave-based methods including UT, PAUT, and EMAT perform well in detecting deep internal defects inside rail head, web, and base regions due to the good penetration

TABLE I
MAIN NDT METHODS FOR RAIL INDUSTRY

| Method | Highest Speed | Defects detected | Deficiency |
|--------------|---------------|---|--|
| UT [6] | 50 mph | Rail head internal defects, rail web and foot defects | Low accuracy for rail head surface defects smaller than 4 mm |
| EMAT [8, 19] | 6 mph | Rail head surface and deep internal defects | Low inspection speed |
| ECT [9] | 180 mph | Rail head surface and near-surface defects | Skin-depth effect, variation of lift-off values |
| MFL [11] | 45 mph | Rail head surface and near-surface defects | Negative effect of MIEC |
| ACFM [12] | 50 mph | Rail head surface breaking defects | Skin-depth effect, cannot detect subsurface defects |
| EMFI [13] | 20 mph | Rail head surface breaking defects | Low accuracy for subsurface defects |

capability of ultrasonic waves [6], [7], while electromagnetic field-based methods including ECT, ECPT, MFL, ACFM, and EMFI are suitable for detecting surface and near-surface RCF defects on the rail head because most electromagnetic fields are concentrated on the material surface [14], [15]. Thus, to get full detection coverage of rail defects at different rail regions in one inspection procedure, one of the current and future research directions is to develop a multi-modal inspection system fusing ultrasonic-based and electromagnetic-based methods [16].

Nowadays, with the continued growth of train speed and transportation mileage as well as dense traffic, railway inspection faces a new challenge of monitoring railroads more efficiently with inspection speeds up to 60 mph or higher [11], [17], [18]. In practice, NDT sensing systems are usually installed on specific rail inspection devices, such as hi-rail vehicles or inspection trains [19]. High-speed NDT sensing systems can significantly improve the detection mileage and efficiency during limited maintenance intervals between dense traffic. However, the existing NDT methods, e.g., UT, magnetic flux leakage (MFL), and ECT, reach their physical limits for high-speed inspection due to negative velocity effect, long excitation and receiving time for NDT sensors, lift-off variations, etc., causing low detection sensitivity and signal-to-noise ratio (SNR). In [15], it was found that speeds of more than 40 mi/h were very close to the limits of conventional UT methods, because the maximum pulse excitation rate was limited by the sound velocity in the railroad, which affected the lateral resolution of UT measurements. In [11] and [17], the effect of velocity-induced eddy currents on the high-speed MFL method was studied, and the results from simulation modeling and field test both indicated that the measured MFL signals were deteriorated due to the velocity effect, and the magnitude of MFL signals decreased about 70% and the SNR decreased about 10 dB for high-speed rail inspection. In [9], the effect of scanning speed on ECT signals was studied through the experiments with a wide speed range of 20–300 km/h, and the results showed that the ECT defect signal amplitude decreased approximately linearly with the increase of speed, which indicated that the inspection speed had a negative effect on the ECT measurements.

Some scholars tried to leverage the high-speed motion between sensing systems and materials as the excitation sources, and measure the response caused by the interaction between the excitation sources and material defects to improve the probability of detection (POD) of defects at high-speed scenarios. In [18], a high-speed passive and noncontact technique-based UT method was proposed to exploit the high-speed rolling train wheels as the acoustic excitation of the rail, and the field test was performed recently which achieved a high speed of 40 mi/h with a POD over 80% under 30% false alarms. In [20], the effect of dynamic magnetization and magnetic hysteresis was considered as the main factor caused by the high-speed motion that altered the intensity and distribution of MFL signals, and a specific high-speed rotational disc platform was developed to verify the dynamic magnetization effect on the high-speed MFL measurements. Recently, studies for adopting the generation and diffusion of motion-induced eddy current (MIEC) as the excitation source were developed. In [21], the authors investigated the MIEC of a dc electromagnetic probe for high-speed crack detection, and the relationships between crack depths and widths were discovered by simulation modeling and rotational disc experiment. In [22] and [23], the presented MIEC method used a probe including a cylindrical permanent magnet and a magnetic sensor which was moved with a constant speed in the vicinity of aluminum plates to detect subsurface defects, and the sensor's geometry, position, and orientation as well as sensing axis and range were discussed and strategically chosen in order to increase detection sensitivity.

This article proposes a horizontal U-shaped magnets-based MIEC array (MIECA) method to detect rail defects for high-speed inspection. In the previous work [17], we analyzed the high-speed rail MFL inspection through the strong N- and S-pole magnets with a large distance of 2 m that the induced MIEC at the middle of the two magnets distorts three-axis MFL signals. Here, the MIECA method employs the horizontal U-shaped magnets with a short distance between the two magnet poles and deploys a three-axis magnetic sensor array along the rail transverse direction at the middle of the magnets to measure the MIECA signals, which utilizes the wake effect of the diffused MIEC caused by the relative high-speed motion between the magnets and the rail track and is found to have a positive effect on the MIECA signals caused by rail surface defects. Comparing to the existing works in [20]–[23] that characterize defects through 1-D curve signals, the horizontal U-shaped magnets-based MIECA method has the potential of obtaining 2-D image signals with three axes, which can provide more information for defect size characterization and profile reconstruction. Finite-element method (FEM) simulations with a wide speed range from 0 to 62.5 mi/h are carried out here to investigate the relationships between the MIEC generation, diffusion, and magnitude and the obtained three-axis image signals. The simulation results show that the higher the speed, the greater the magnitude of diffused MIEC, and the greater the peak-to-peak values of MIECA signals, which shows a great promise for detecting rail surface defects in high-speed scenarios. The characteristics of 2-D MIECA image signals relative to the defect profile and

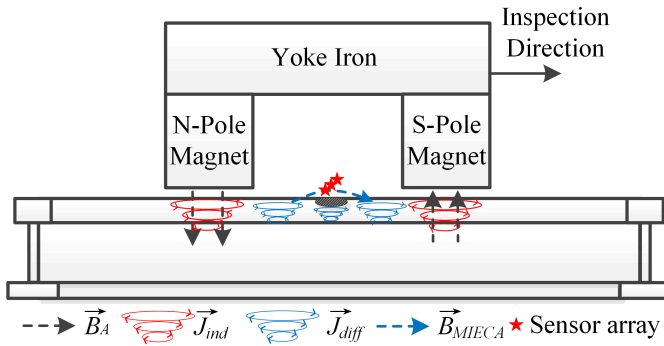


Fig. 2. Schematic of MIECA method using horizontal U-shaped magnets during high-speed rail inspection.

the detection sensitivity for different speeds are also presented and discussed.

The rest of this article is organized as follows: Section II presents the mechanism of the horizontal U-shaped magnets-based MIECA method during high-speed rail inspection. Section III presents the FEM simulation models, results and discussions, followed by conclusions and future work summarized in Section IV.

II. MECHANISM OF MIECA METHOD

The inspection principle of the horizontal U-shaped magnets-based MIECA method is shown in Fig. 2. The magnetizing system includes N- and S-pole magnets and yoke iron, which moves forward along the rail horizontal direction (y -direction). The two magnets generate applied dc magnetic fields \vec{B}_A that magnetize the rail track along the rail vertical direction (z -direction) as denoted by the black dashed arrows shown in Fig. 2. The relationship between magnetic flux density (MFD) \vec{B}_A and applied magnetic field strength \vec{H}_A inside the rail track is given by

$$\vec{B}_A = \mu \vec{H}_A = \mu_0 \mu_{r(BH)} \vec{H}_A = \mu_0 (\vec{H}_A + \vec{M}) \quad (1)$$

where \vec{M} is the magnetization of rail track, μ_0 is the permeability of vacuum, and $\mu_{r(BH)}$ is the relative permeability of the rail track, which follows the $B-H$ curve of ferromagnetic materials. In contrast to the rail MFL method discussed in [11] and [17], the main goal of the magnetizing system here is not to magnetize the rail track to its saturation where MFL signals can be generated, but to provide the source of MIEC excitation. From Maxwell's equations, the governing equation for the induced eddy currents in the rail track is written as [17], [24], [25]

$$\nabla \times \left(\frac{1}{\mu} \nabla \times \vec{A} \right) = \vec{J}_S - \sigma \frac{\partial \vec{A}}{\partial t} + \sigma \vec{V} \times \nabla \times \vec{A} \quad (2)$$

where \vec{J}_S is source current density, σ is the electrical conductivity, \vec{A} is the magnetic vector potential, and \vec{V} is inspection velocity. For the horizontal U-shaped magnetizing system using the permanent magnets with a short distance between the two poles, since there is no time-varying magnetic field, the induced eddy current in the rail track caused

by the time-varying component $(\partial \vec{A} / \partial t)$ can be ignored. Then, the main component of induced eddy currents is caused by the applied dc magnetic field $\vec{B}_A = \nabla \times \vec{A}$, perpendicular to the inspection velocity, thus, the induced MIEC in the rail track can be defined as

$$\vec{J}_{\text{ind}} = \sigma \vec{V} \times \vec{B}_A = \sigma \vec{V} \times \nabla \times \vec{A}. \quad (3)$$

The induced MIEC is mainly generated under the two magnet poles. Due to the wake effect caused by the diffusion of eddy currents as well as the high-speed motion, the induced MIEC under the two poles will not disappear immediately but gradually diffuse over time. The eddy current diffusion equations are written as follows, where the derivation can be found in [26] and [27]

$$\frac{1}{\sigma \mu} \nabla^2 \vec{J}_{\text{diff}} = \frac{\partial \vec{J}_{\text{diff}}}{\partial t} \quad (4)$$

$$\vec{J}_{\text{diff}}|_{t=0} = \vec{J}_{\text{ind}} \quad (5)$$

where the diffusion coefficient is defined as $\gamma = (1/\sigma \mu)$, which indicates how fast the diffusion process is. The MIECA method uses the wake effect of diffused MIEC at the middle of two poles as the excitation source for the rail RCF defect detection, as shown in Fig. 2. Here, the diffused MIEC \vec{J}_{diff} is a function of the magnetic vector potential, inspection velocity, and diffusion coefficient written as

$$\vec{J}_{\text{diff}}(\mathbf{x}, t) = f(\vec{A}, \vec{V}, \gamma) = \int_{R^n} G(\mathbf{x} - \mathbf{y}, t) \vec{J}_{\text{ind}}(\mathbf{y}) d\mathbf{y} \quad (6)$$

where Green's function is written as

$$G(\mathbf{x} - \mathbf{y}, t) = \frac{1}{\sqrt{(4\pi \gamma t)^n}} \exp\left(-\frac{(\mathbf{x} - \mathbf{y}) \cdot (\mathbf{x} - \mathbf{y})}{4\gamma t}\right). \quad (7)$$

The magnitude of diffused MIEC is one of the main factors that determine the detection sensitivity of the MIECA method. In terms of \vec{J}_{ind} , the higher the velocity, the greater the magnitude of \vec{J}_{ind} as indicated by (3), and the greater the magnitude of \vec{J}_{diff} . In terms of \vec{V} , the higher the velocity, the shorter the diffusion time for \vec{J}_{ind} under the two magnet poles to diffuse to be \vec{J}_{diff} at the middle of the two poles, so that the greater the magnitude of \vec{J}_{diff} . In terms of γ , the rail track has a high conductivity (e.g., 5×10^6 S/m) and permeability (e.g., $\mu_r = 200$) that makes γ lower than non-ferromagnetic materials, which indicates the diffusion process is relatively slow and is also helpful to obtain a greater magnitude of \vec{J}_{diff} . Thus, the (6) and (7) indicate that the higher the speed, the greater the magnitude of \vec{J}_{diff} for the high-speed rail MIECA inspection.

For the magnetic field distributions $\vec{B}_{\text{non-defect}}$ at non-defect cases, there are three main components including primary magnetic field \vec{B}_A , secondary magnetic field \vec{B}_{ind} generated by \vec{J}_{ind} , and secondary magnetic field \vec{B}_{diff} generated by \vec{J}_{diff} . For \vec{B}_{defect} at defect cases, when the center of the magnetizing system passes over a rail defect as shown in Fig. 2, the existence of the defect will cause a disturbance to the diffused MIEC denoted as $\vec{J}'_{\text{diff}} = \vec{J}_{\text{diff}} + \vec{J}_{\text{dist}}$, where \vec{J}_{dist} is the disturbance component. Then, the secondary magnetic field \vec{B}_{diff} is changed to be $\vec{B}'_{\text{diff}} = \vec{B}_{\text{diff}} + \vec{B}_{\text{dist}}$, where \vec{B}_{dist} is generated by \vec{J}_{dist} . Thus, the measured MIECA signal which

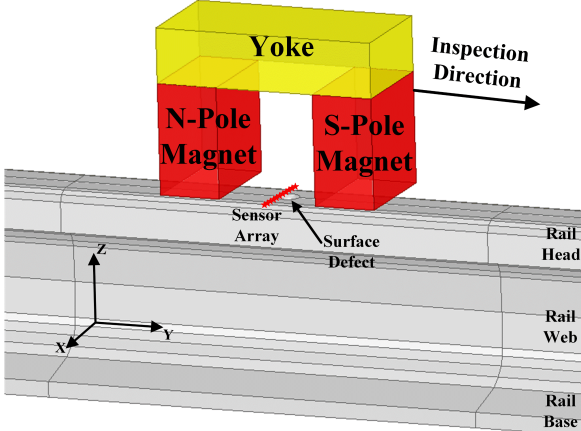


Fig. 3. Simulation model of MIECA method for rail surface defect detection.

is used to characterize rail defects is defined as the measured magnetic fields of defect cases subtracting non-defect cases as follows:

$$\begin{aligned} \vec{B}_{\text{MIECA}} &= \vec{B}_{\text{defect}} - \vec{B}_{\text{non-defect}} = \left(\vec{B}_A + \vec{B}_{\text{ind}} + \vec{B}'_{\text{diff}} \right) \\ &\quad - \left(\vec{B}_A + \vec{B}_{\text{ind}} + \vec{B}_{\text{diff}} \right) \\ &= \vec{B}'_{\text{diff}} - \vec{B}_{\text{diff}} = \vec{B}_{\text{dist}}. \end{aligned} \quad (8)$$

For the practical application, it is noted that the subtraction between the two cases should be performed at the same inspection speed, because the two components \vec{B}_{ind} and \vec{B}_{diff} are related to the inspection speed as described from (3) to (8). Thus, the two components can be counteracted at the same inspection speed so that the measured MIECA signal is only related to the disturbance component \vec{B}_{dist} . Since the disturbance component \vec{B}_{dist} is generated by \vec{J}_{dist} that is directly related to the defect geometry and \vec{J}_{diff} , while the current density of \vec{J}_{diff} increases with the increase of inspection speed as described in (3) and (6), thus, from the perspective of inspection principle, the horizontal U-shaped magnets-based MIECA method has the potential to provide high-speed high-sensitivity (HSHS) capability for detecting rail defects in high-speed scenarios. The characteristics of these physical parameters, the distributions of induced MIEC and diffused MIEC, and the measured MIECA signals at different speed cases are further studied quantitatively through the following FEM simulations.

III. NUMERICAL MODELING AND RESULTS

A. Simulation Setup

The simulation model of the horizontal U-shaped magnets-based MIECA method for rail surface defect detection is shown in Fig. 3. The simulations are implemented using Ansys Maxwell software version 19. The magnetizing system consists of two permanent magnets with opposite polarities and a yoke. Unlike the traditional MFL method with a large distance, i.e., greater than 2 m between the two magnet poles [11], [17], the MIECA method utilizes a short distance as small as 145 mm. The lift-off distance between the two magnets and the rail head surface is 10 mm. A hemisphere

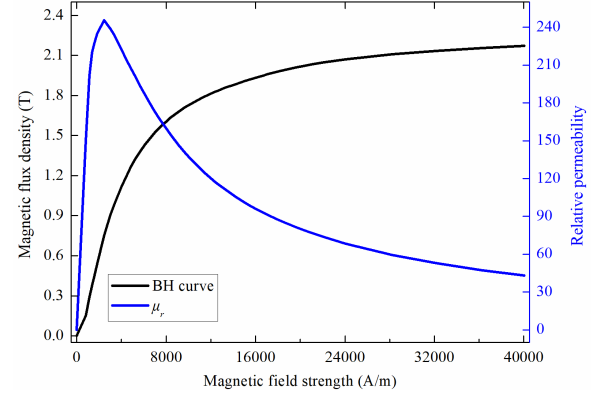
Fig. 4. Nonlinear B - H curve of the rail track.

TABLE II
MAIN MATERIAL PARAMETERS SETTING

| Conductivity of Rail | Magnetic Coercivity of Magnets | Relative Permeability of Yoke |
|----------------------|--------------------------------|-------------------------------|
| 5×10^6 S/m | 7.2×10^5 A/m | 1000 |

defect is introduced on the rail head surface to represent rail RCF squat-type damages which is one of the typical RCF damages. The magnetic sensor array marked as red stars in Fig. 3 is at the middle of the two magnets with a lift-off value of 1 mm, and the interval of each magnetic sensor is set to be 1 mm, which can measure the three-axis magnetic fields in space. The element length-based refinement method is applied to mesh the model components, and the minimum edge length of the rail track model is 0.5 mm, and the total number of model elements is over 1800000. In practice, the sensing system will be integrated into a specific rail inspection device, such as a hi-rail vehicle or inspection train, to perform in-motion detection along the rail horizontal direction. In the simulations, the magnetic transient solution type is selected to calculate the transient magnetic fields caused by the in-motion inspection. The zero tangential H -field boundary is assigned to the outermost boundaries of air region which is placed far from the rail track and MIECA sensing models. To consider the MIECs generated in the rail track, the eddy effect excitation is applied to the rail track, and the sensing system including magnets, yoke, and sensor array is inside a motion band to generate a horizontal movement along the positive y -axis as shown in Fig. 3. Then, along with the motion, the magnetic sensor array can obtain the MIECA signals caused by the defect as 2-D image signals. The inspection speed considered here is from 0 to 62.5 mi/h with eight different cases to investigate the relationships between MIECA signals and inspection speeds. Fig. 4 shows the nonlinear B - H curve as well as relative permeability curve of the rail track set in the simulations. The material parameters of the numerical models are listed in Table II, and the size parameters are listed in Table III.

B. Distributions of MIEC and Magnetic Fields

Fig. 5(1a)–(1f) show the distributions of MIEC in the horizontal central cross-section of the rail head at the six

TABLE III
SIZE PARAMETERS SETTING

| Parameters | Values |
|----------------------------------|--|
| Length of rail | 3 m |
| Height of rail | 175 mm |
| Width of rail base | 150 mm |
| Width of rail head | 72 mm |
| Length of magnet | 55 mm |
| Height of magnet | 100 mm |
| Length of yoke | 200 mm |
| Height of yoke | 50 mm |
| Width of magnet and yoke | 100 mm |
| Distance between two poles | 145 mm |
| Radius of hemisphere-type defect | 10 mm |
| Depth of hemisphere-type defect | 6 mm |
| Inspection speeds | 0, 3.125, 6.25, 12.5, 25, 37.5, 50, 62.5 mph |

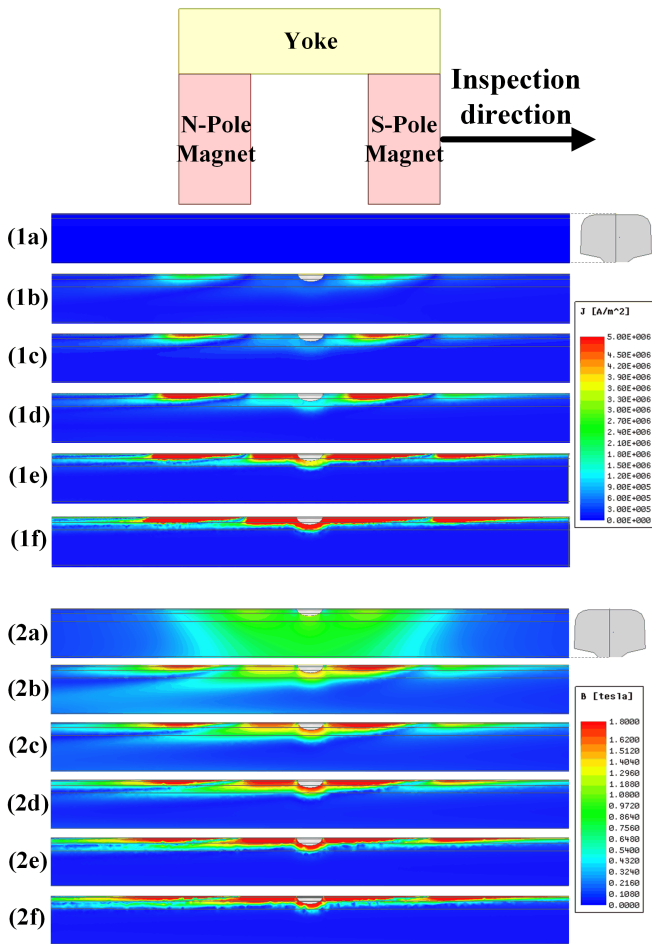


Fig. 5. Distributions of MIEC and MFD in horizontal central cross-section of rail head at different inspection speeds. (1a) 0 mi/h. (1b) 3.125 mi/h of MIEC. (1c) 6.25 mi/h of MIEC. (1d) 12.5 mi/h of MIEC. (1e) 37.5 mi/h of MIEC. (1f) 62.5 mi/h of MIEC. (2a) 0 mi/h of MFD. (2b) 3.125 mi/h of MFD (2c) 6.25 mi/h of MFD. (2d) 12.5 mi/h of MFD. (2e) 37.5 mi/h of MFD. (2f) 62.5 mi/h of MFD.

different inspection speeds, while Fig. 5(2a)–(2f) show the distributions of MFD. For the static case of 0 mi/h, the current density of MIEC is 0 because the velocity component is 0 as described by (3). As the inspection speed increases,

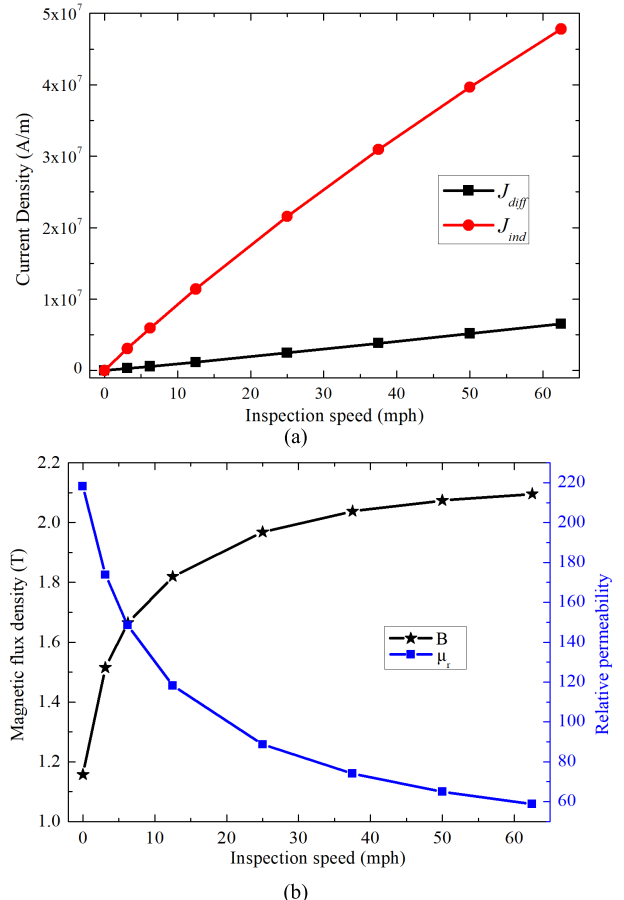


Fig. 6. Current density of MIEC and MFD change with inspection speed. (a) Current densities of J_{ind} and J_{diff} change with inspection speed. (b) MFD and relative permeability change with inspection speed.

the current density and distribution areas of MIEC become larger, including \vec{J}_{ind} under the two poles and \vec{J}_{diff} at the middle of the two poles. For the low-speed cases such as those shown in Fig. 5(1b)–(1d), the wake effect of diffusion is not obvious that the magnitude of \vec{J}_{diff} is relatively low. For the high-speed cases shown in Fig. 5(1e) and (1f), as the magnetizing system moves faster, the wake effect of diffusion shows up clearly that a strong magnitude of \vec{J}_{diff} distributed at the middle area near the rail surface defect. Then, the existence of the defect causes a disturbance to the \vec{J}_{diff} that \vec{J}_{diff} is distributed surrounding the defect. Meanwhile, the current densities of \vec{J}_{ind} and \vec{J}_{diff} changing with inspection speed is shown in Fig. 6(a). For the same speed, the current density of \vec{J}_{ind} is much greater than that of \vec{J}_{diff} , and both increase linearly with the increase of inspection speed.

As shown in Fig. 5(2a), for the static case of 0 mi/h, the dominant component of the magnetic field in the rail track is \vec{B}_A , which is the applied dc magnetic field generated by the two magnets; thus, it is distributed uniformly and symmetrically, and the magnitude is around 1.15 T. Then, the MFD and relative permeability of the rail track changing with inspection speed are shown in Fig. 6(b). The higher the speed, the greater the MFD and the lower the relative permeability. For the in-motion inspection cases as shown in Fig. 5(2b)–(2f), the magnetic fields in the rail track are

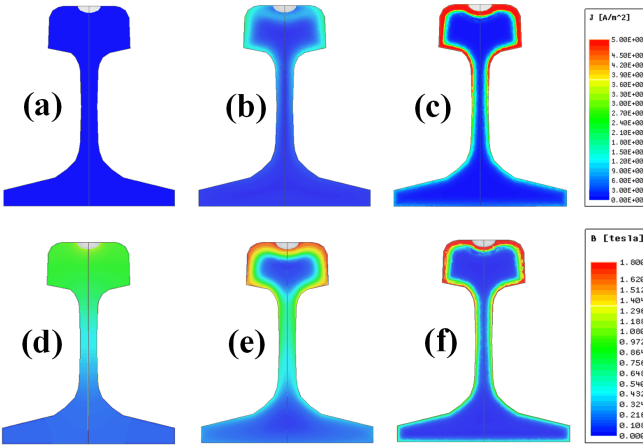


Fig. 7. Distributions of diffused MIEC and MFD along right-side view in rail transverse section at the center of defect under different inspection speeds. (a) 0 mi/h. (b) 6.25 mi/h of diffused MIEC. (c) 62.5 mi/h of diffused MIEC. (d) 0 mi/h of MFD. (e) 6.25 mi/h of MFD. (f) 62.5 mi/h of MFD.

the superposition of \vec{B}_A and the secondary magnetic fields \vec{B}_{ind} and \vec{B}_{diff} . Figs. 5 and 6 show that the higher the speed, the greater the magnitude of \vec{J}_{ind} and \vec{J}_{diff} , so that the greater the magnitude of \vec{B}_{ind} and \vec{B}_{diff} . It is worth noting that the secondary magnetic fields become the major components of magnetic fields in the rail track for the higher speed cases as shown in Fig. 5(2e) and (2f) comparing to the static case of Fig. 5(2a), which is one of the main difference between the high-speed rail MIECA method and the high-speed rail MFL method [11], [17]. More specifically, for the MFL method, \vec{B}_A is used to magnetize the rail track to saturation while the secondary magnetic fields are generated to counteract \vec{B}_A to exit the magnetic saturation zone. In contrast, for the MIECA method, \vec{B}_A is used to be the excitation source for the MIEC generation, while the secondary magnetic fields are generated to further magnetize the rail head surface to its saturation zone where the MFD is over 2.0 T when the speed is over 40 mi/h as shown in Fig. 6(b).

The other two viewing angles including right-side view and top view as well as vector distributions of MIEC and magnetic fields are presented and analyzed here, which help us understand the MIEC distributions inside the rail head. Fig. 7(a)–(c) shows the distributions of diffused MIEC along the right-side view in the rail transverse section at the center of the defect under the three different speeds, while Fig. 7(d), (e), and (f) shows the distributions of MFD. With the increase of speed, the current density of \vec{J}_{diff} increases. Meanwhile, \vec{J}_{diff} is mainly distributed on the surface of rail head with a low penetration depth due to the skin effect, so that the current density of \vec{J}_{diff} inside the rail head is close to zero. As shown in Fig. 7(d), when the speed is 0 mi/h, there is no MIEC distributed in the rail track, thus, the magnet field is distributed uniformly inside the rail head, which has the same characteristic shown in Fig. 5(2a). When the speed increases, the secondary magnetic field \vec{B}_{diff} generated by \vec{J}_{diff} becomes the dominant component, and the higher the speed, the greater the MFD on the rail surface. Since the distribution of \vec{J}_{diff} exhibits the skin effect characteristic, \vec{B}_{diff} is gradually

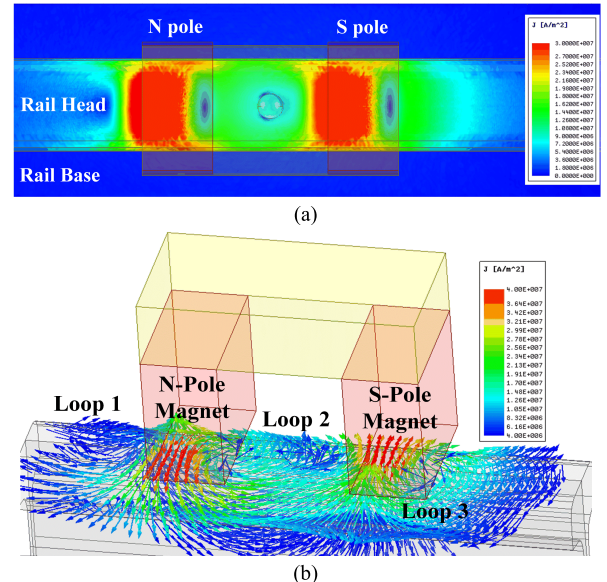


Fig. 8. Distributions of MIEC on rail head surface when speed is 62.5 mi/h. (a) Top-side view. (b) Vector distribution.

concentrated on the surface of the rail head, and that inside the rail head is close to 0.

Fig. 8(a) shows the MIEC distribution on the rail surface along the top-side view at high-speed case of 62.5 mi/h, and Fig. 8(b) shows the corresponding vector distribution of MIEC. As shown in Fig. 8(a), there are three areas showing the wake effect of diffusion, including the area behind the N-pole magnet, the area at the middle of the two poles, and the area front of the S-pole magnet, which are also denoted by Loop 1, Loop 2, and Loop 3 in Fig. 8(b), respectively. Since Loop 2 is distributed more uniformly and the current density of Loop 2 is greater than that of Loop 1 and Loop 3, thus, the structure of horizontal U-shaped magnets utilizing Loop 2 to detect MIECA signals can provide a better HSHS capability than only using one permanent magnet [22], [23]. The vector distribution where the existence of the rail surface defect causes the disturbance component \vec{J}_{dist} to the \vec{J}_{diff} is shown clearly in Loop 2 in Fig. 8. The secondary magnetic fields generated by \vec{J}_{dist} are measured by the magnetic sensor array to obtain MIECA signals.

C. Three-Axis MIECA Signals

Fig. 9 shows the transverse x -axis MIECA signals from the magnetic sensor array at different speeds. For the static case of 0 mi/h, the measured image signal is only caused by \vec{B}_A because the current density of MIEC is 0, and the main component is the MFL signal, which has two positive peaks and two negative peaks, and the four peaks are symmetrically distributed on the diagonal. With the increase of inspection speed, the MIEC component becomes dominant, and the two peaks on the left gradually disappear due to the superposition of \vec{B}_{dist} . For the high-speed case of 62.5 mi/h, there are two main peaks distributed symmetrically along the x -axis. Meanwhile, the color bars on the right show that the magnitude of peaks for the case of 0 mi/h is about 4×10^{-3} T, while that

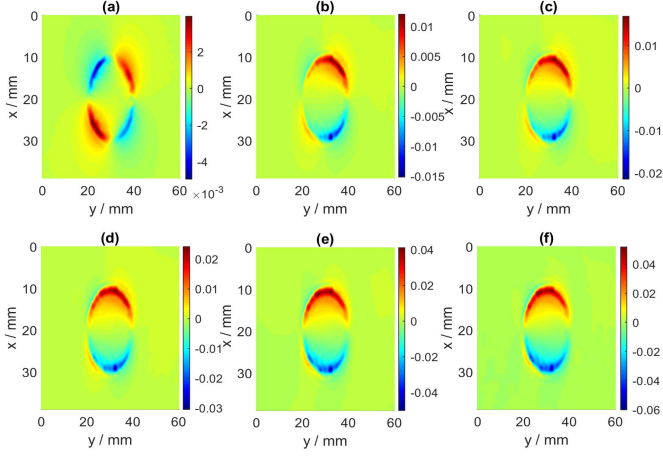


Fig. 9. MIECA signals along x -axis transverse direction at different speeds. (a) 0 mi/h. (b) 3.125 mi/h. (c) 6.25 mi/h. (d) 12.5 mi/h. (e) 37.5 mi/h. (f) 62.5 mi/h.

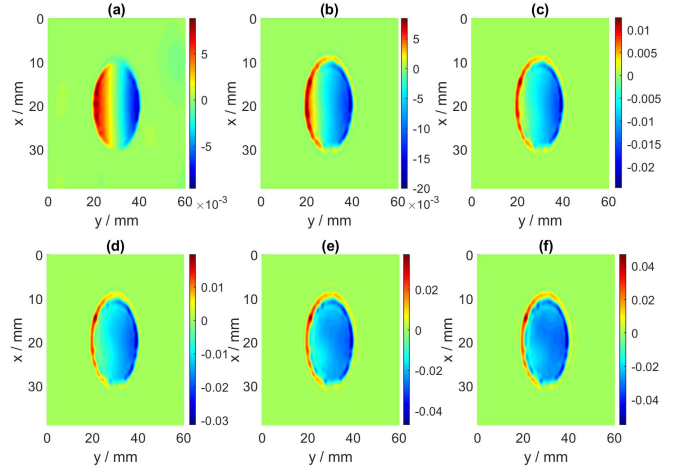


Fig. 11. MIECA signals along z -axis vertical direction at different speeds. (a) 0 mi/h. (b) 3.125 mi/h. (c) 6.25 mi/h. (d) 12.5 mi/h. (e) 37.5 mi/h. (f) 62.5 mi/h.

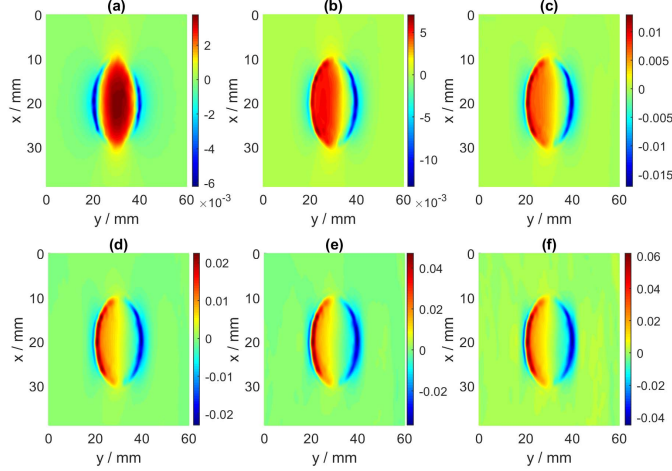


Fig. 10. MIECA signals along y -axis horizontal direction at different speeds. (a) 0 mi/h. (b) 3.125 mi/h. (c) 6.25 mi/h. (d) 12.5 mi/h. (e) 37.5 mi/h. (f) 62.5 mi/h.

for the case of 62.5 mi/h is about 0.04 T, which means the magnitude of MIECA signals increases an order from static case to high-speed case. Fig. 10 shows the horizontal y -axis MIECA signals at different speeds. For the static case, there is one positive peak located at the middle and two negative peaks located on both sides, which are distributed symmetrically along the y -axis. With the increase of speed, the negative peak on the left gradually disappears, and the positive peak at the middle is shifted to the left. Then, Fig. 11 shows the vertical z -axis MIECA signals at different speeds. When the speed is 0 mi/h, there are one positive peak and one negative peak distributed symmetrically along the y -axis, while the symmetrical property is gradually disappeared with the increase of speed. Figs. 9–11 indicate that the magnitudes of three-axis MIECA signals increase a lot when the inspection speed increases, and the shapes of three-axis MIECA signals have changed significantly from static cases to high-speed cases. Meanwhile, the radius of the hemisphere-type defect is 10 mm, and the center of the defect is located at the center of the image signals,

then, Figs. 11 also shows that the three-axis MIECA image signals can characterize the defect profile well.

Fig. 12(a)–(c) further shows the 1-D MIECA curve signals extracted from Figs. 9–11 to analyze the peak values changing with the speed. Fig. 12(a) shows the transverse component extracted from Fig. 9 at $y = 38$ mm along the transverse direction. The peak-to-peak values of MIECA signals are increased with the increase of inspection speed. Meanwhile, the positive peaks are located at $x = 13$ mm and the negative peaks are located at $x = 27$ mm. The distance between the two peaks is almost the same for different speeds, which means that the distance between the two peaks is basically not affected by the inspection speed. Fig. 12(b) shows the horizontal component extracted from Fig. 10 at $x = 20$ mm along the horizontal direction, while Fig. 12(c) shows the vertical component extracted from Fig. 11 at $x = 20$ mm along the horizontal direction. The results show that the characteristics of peak values from Fig. 12(b) and (c) are basically the same as Fig. 12(a).

D. Discussion

Fig. 13 extracts the peak-to-peak values of three-axis MIECA signals from the same hemisphere rail surface defect changing with different speeds. Take the y -axis MIECA signals as an example, the peak-to-peak values are increased from 0.01 T at 0 mi/h to over 0.1 T at 62.5 mi/h, which shows a great promise for detecting surface defects in rails in high-speed scenarios. To study the influence of lift-off distance on the magnetic sensors reading, the peak-to-peak values of MIECA signals changing with lift-off values at speed of 62.5 mi/h are shown in Fig. 14. The peak-to-peak values decrease gradually with the increase of lift-off values, resulting in a decrease of more than 60% from 1 to 5 mm. Thus, the lift-off distance is an important factor that affects the MIECA measurements, which needs to be considered in the practical application. To study the relationship between MIECA signal characteristics and defect sizes, a set of narrow long crack-shaped defects with a length of 40 mm (x -axis), a width of

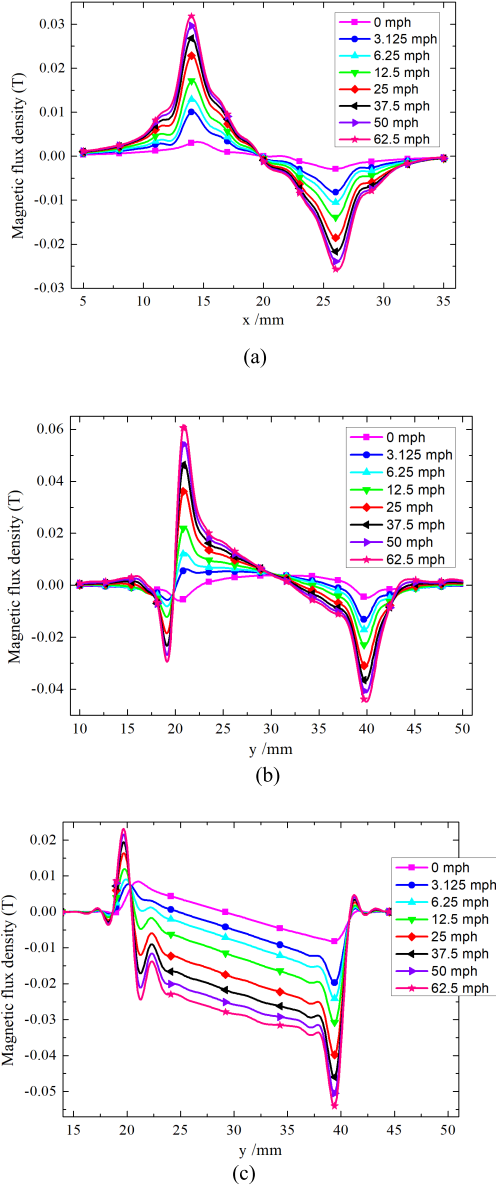


Fig. 12. 1-D MIECA signals along three axes at different speeds. (a) x-axis transverse direction. (b) y-axis horizontal direction. (c) z-axis vertical direction.

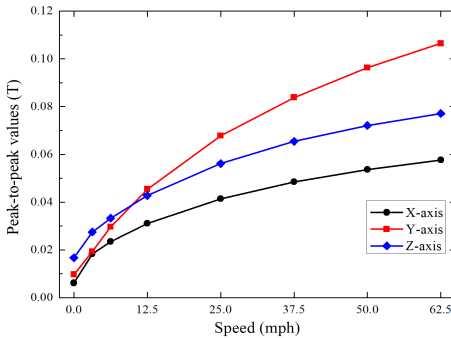


Fig. 13. Peak-to-peak values of three-axis MIECA signals at different speeds.

5 mm (y-axis), and different depths ranging from 1 to 10 mm (z-axis) are further simulated using the presented horizontal U-shaped magnets-based MIECA model, and the result of peak-to-peak values of z-axis MIECA signals changing with

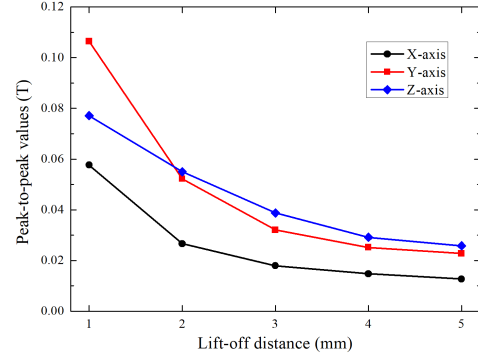


Fig. 14. Peak-to-peak values of three-axis MIECA signals change with lift-off distance.

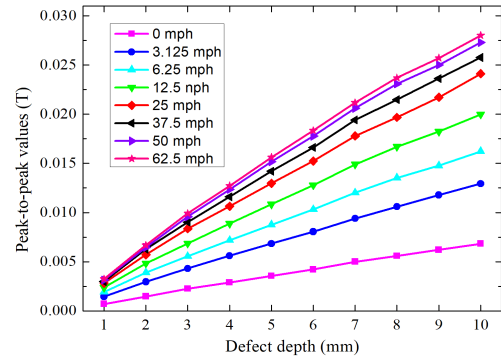


Fig. 15. Peak-to-peak values of z-axis MIECA signals change with defect depths and inspection speeds.

the defect depths and inspection speeds are shown in Fig. 15. It can be seen that the peak-to-peak values increase linearly with the growth of defect depths for different speed cases, which is helpful for defect detection and depth quantification. If we define the slope of each line as the detection sensitivity of the MIECA method, which means that every 1 mm increase in the defect depth corresponds to the increase of MIECA signal magnitude measured by the magnetic sensor array. Then, Fig. 15 shows that the higher the speed, the higher the detection sensitivity of the MIECA method, and the detection sensitivity is increased about four times from 0.0007 T/mm at 0 mi/h to 0.0028 T/mm at 62.5 mi/h, which indicates that the horizontal U-shaped magnets-based MIECA method can provide the HSIS capability for detecting rail surface defects.

The contributions of this article compared with the existing NDT methods are discussed here. As presented in the previous work [17], the mechanism of the high-speed rail MFL method is based on the magnetization of rail track through the applied strong dc magnetic field to measure the magnetic leakage fields, while the induced MIEC reduces the level of magnetization so that it has the negative effect on the MFL measurements in high-speed scenarios. In this article, we utilize the horizontal U-shaped magnets with a short distance between the two magnet poles to take advantage of the diffused MIEC as the main excitation source. In this case, the greater the diffused MIEC, the better the signal measurements. Then, Fig. 6(a) shows that the current density of diffused MIEC increases

linearly with the increase of inspection speed, which is the main reason that the MIECA method can provide the HSHS capability. One may consider putting the magnetic sensors near the magnet poles since the current density near the magnet poles is much larger than that at the middle area. This idea has been validated in [21] and [23] where in [21] the sensors are located inside a dc coil and in [23] the sensors are located right behind a permanent magnet, and the results both show the HSHS capability. The issue that needs to be considered for this structure is that the superposition of the applied dc magnetic field may cause a large shift on the base values or exceed the range of magnetic sensors because the magnetic sensors are too close to the permanent magnets. Here, the proposed MIECA method with the structure of horizontal U-shaped magnets with the sensor array at the middle can mitigate the influence of applied dc magnetic field that has the potential to measure high-quality 2-D image signals. Figs. 9–11 also show that the MIECA image signals from the horizontal U-shaped magnets-based model can characterize the defect profile well, which can provide more useful information for defect profile reconstruction.

IV. CONCLUSION

HSHS inspection of rail RCF defects using NDT methods is important to the safety of railway transportation. Most existing NDT methods suffer from a bottleneck in that a higher inspection speed causes a lower detection sensitivity due to their physical limits, such as the negative velocity effect. To obtain an improved detection sensitivity at high speeds, this article proposes the horizontal U-shaped magnets-based MIECA method to detect rail surface defects in high-speed scenarios. The MIECA method utilizes the wake effect of diffused MIEC at the middle of two magnet poles as the source of MIEC measurements. The simulation results show that the higher the speed, the greater the magnitude of diffused MIEC, and the greater the peak-to-peak values of three-axis MIECA signals, and the greater the detection sensitivity of the MIECA method, which shows a great promise for detecting rail surface defects in high-speed scenarios and is superior inspection relative to existing NDT methods. The future work will focus on the high-speed rail MIECA inspection experiments and validations, as well as the data inverse algorithms based on the measured MIECA signals to quantify the defect sizes and reconstruct defect profiles.

ACKNOWLEDGMENT

This work was partially supported by the AAR Strategic Research Initiative (SRI) University Program. The authors would like to thank the support of the Association of American Railroads/Transportation Technology Center, Inc. (AAR/TTCI), Pueblo, CO, USA. They would also like to thank Dr. Anish Poudel for his valuable comments.

REFERENCES

- [1] S. Liu, Q. Wang, and Y. Luo, “A review of applications of visual inspection technology based on image processing in the railway industry,” *Transp. Saf. Environ.*, vol. 1, no. 3, pp. 185–204, Dec. 2019.
- [2] S. S. Artagan, L. B. Ciampoli, F. D’Amico, A. Calvi, and F. Tosti, “Non-destructive assessment and health monitoring of railway infrastructures,” *Surv. Geophys.*, vol. 41, no. 3, pp. 447–483, May 2020.
- [3] M. Steenbergen, “Rolling contact fatigue: Spalling versus transverse fracture of rails,” *Wear*, vols. 380–381, pp. 96–105, Jun. 2017.
- [4] X. Liu, M. R. Saat, and C. P. L. Barkan, “Analysis of causes of major train derailment and their effect on accident rates,” *Transp. Res. Rec., J. Transp. Res. Board*, vol. 2289, no. 1, pp. 154–163, 2012.
- [5] M. Rakos, “The origins of practical electromagnetic testing and the historical contributions of magnetic analysis corporation to non-destructive testing,” *e-J. Nondestruct. Test.*, vol. 24, no. 6, pp. 1–14, 2019.
- [6] A. Poudel, B. Lindeman, and R. Wilson, “Current practices of rail inspection using ultrasonic methods: A review,” *Mater. Eval.*, vol. 77, no. 7, pp. 870–883, 2019.
- [7] G. Kim, M.-K. Seo, Y.-I. Kim, S. Kwon, and K.-B. Kim, “Development of phased array ultrasonic system for detecting rail cracks,” *Sens. Actuators A, Phys.*, vol. 311, Aug. 2020, Art. no. 112086.
- [8] P. A. Petcher, M. D. G. Potter, and S. Dixon, “A new electromagnetic acoustic transducer (EMAT) design for operation on rail,” *NDT & E Int.*, vol. 65, pp. 1–7, Jul. 2014.
- [9] P. Xu, C. Zhu, H. Zeng, and P. Wang, “Rail crack detection and evaluation at high speed based on differential ECT system,” *Measurement*, vol. 166, Dec. 2020, Art. no. 108152.
- [10] J. Zhu *et al.*, “Characterization of rolling contact fatigue cracks in rails by eddy current pulsed thermography,” *IEEE Trans. Ind. Informat.*, vol. 17, no. 4, pp. 2307–2315, Apr. 2021.
- [11] A. G. Antipov and A. A. Markov, “3D simulation and experiment on high speed rail MFL inspection,” *NDT & E Int.*, vol. 98, pp. 177–185, Sep. 2018.
- [12] M. P. Papaelias, M. C. Lugg, C. Roberts, and C. L. Davis, “High-speed inspection of rails using ACFM techniques,” *NDT & E Int.*, vol. 42, no. 4, pp. 328–335, 2009.
- [13] A. M. P. MWitte, P. Gies, and D. Skow, “Rolling contact damage characterization on railroad rails using electromagnetic field imaging,” *Mater. Eval.*, vol. 77, no. 7, pp. 951–965, 2019.
- [14] H.-M. Thomas, T. Heckel, and G. Hanspach, “Advantage of a combined ultrasonic and eddy current examination for railway inspection trains,” *Insight-Non-Destructive Test. Condition Monit.*, vol. 49, no. 6, pp. 341–344, 2007.
- [15] T. Heckel, H.-M. Thomas, M. Kreutzbruck, and S. Rühe, “High speed non-destructive rail testing with advanced ultrasound and eddy-current testing techniques,” in *Proc. NDTIP*, Prague, Czech Republic, 2009, pp. 1–10.
- [16] T. Szugs *et al.*, “Combination of ultrasonic and eddy current testing with imaging for characterization of rolling contact fatigue,” in *Proc. 19th WCNDT*, 2016, p. 19680.
- [17] G. Piao, J. Li, L. Udma, S. Udma, and Y. Deng, “The effect of motion-induced eddy currents on three-axis MFL signals for high-speed rail inspection,” *IEEE Trans. Magn.*, vol. 57, no. 4, pp. 1–11, Apr. 2021.
- [18] A. Liang, S. Sternini, M. Capriotti, and F. L. D. Scalea, “High speed ultrasonic rail inspection by passive noncontact technique,” *Mater. Eval., Special Issue NDT Railroads*, vol. 77, no. 7, pp. 941–950, 2019.
- [19] M. Ph Papaelias, C. Roberts, and C. L. Davis, “A review on non-destructive evaluation of rails: State-of-the-art and future development,” *Proc. Inst. Mech. Eng. F, J. Rail Rapid Transit*, vol. 222, no. 4, pp. 367–384, Jul. 2008.
- [20] P. Wang, Y. Gao, G. Tian, and H. Wang, “Velocity effect analysis of dynamic magnetization in high speed magnetic flux leakage inspection,” *NDT & E Int.*, vol. 64, pp. 7–12, Jun. 2014.
- [21] F. Yuan, Y. Yu, L. Li, and G. Tian, “Investigation of DC electromagnetic-based motion induced eddy current on NDT for crack detection,” *IEEE Sensors J.*, vol. 21, no. 6, pp. 7449–7457, Mar. 2021.
- [22] T. J. Rocha, H. G. Ramos, A. L. Ribeiro, and D. J. Pasadas, “Evaluation of subsurface defects using diffusion of motion-induced eddy currents,” *IEEE Trans. Instrum. Meas.*, vol. 65, no. 5, pp. 1182–1187, May 2016.
- [23] T. J. Rocha, H. G. Ramos, A. L. Ribeiro, and D. J. Pasadas, “Magnetic sensors assessment in velocity induced eddy current testing,” *Sens. Actuators A, Phys.*, vol. 228, pp. 55–61, Jun. 2015.
- [24] G. Piao, J. Guo, T. Hu, and H. Leung, “The effect of motion-induced eddy current on high-speed magnetic flux leakage (MFL) inspection for thick-wall steel pipe,” *Res. Nondestruct. Eval.*, vol. 31, no. 1, pp. 48–67, Jan. 2020.
- [25] W. Lord, S. S. Udma, L. Udma, Y. Sun, and S. Yang, “Application of perturbation methods in finite element analysis of stress corrosion cracking,” *IEEE Trans. Magn.*, vol. 36, no. 4, pp. 1714–1718, Jul. 2000.

- [26] I. D. Mayergoyz, *Nonlinear Diffusion of Electromagnetic Fields: With Applications to Eddy Currents and Superconductivity*. Amsterdam, The Netherlands: Elsevier, 1998.
- [27] P. A. Stucky, "Diffusion effects in eddy current nondestructive evaluation," Ph.D. dissertation, Dept. Elect. Comput. Eng., Iowa State Univ., Ames, IA, USA, 1991.

Guanyu Piao received the B.S. degree in electrical engineering from Jilin University, Changchun, China, in 2014, and the Ph.D. degree in electrical engineering from Tsinghua University, Beijing, China, in 2019.

He is currently a Post-Doctoral Research Fellow with the Nondestructive Evaluation Laboratory, Electrical and Computer Engineering Department, College of Engineering, Michigan State University, East Lansing, MI, USA. His current research interests include electromagnetic, ultrasonic, and optical nondestructive testing and evaluation (NDT&E), applied electromagnetics, machine-learning algorithms, computational modeling, and the development of various NDT systems.

Jiaoyang Li received the B.S. degree in instrument science and technology and the B.A. degree in German from Jilin University, Changchun, China, in 2014, and the Ph.D. degree in the electromagnetic field and microwave technology from the University of Chinese Academy of Sciences, Beijing, China, in 2019.

She is currently a Post-Doctoral Research Fellow with the Nondestructive Evaluation Laboratory, Electrical and Computer Engineering Department, College of Engineering, Michigan State University, East Lansing, MI, USA. Her research interests include electric field, microwave, ultrasonic and optical nondestructive testing and evaluation (NDT&E), machine-learning algorithms, computational modeling, microwave radiometer calibration and analysis, atmospheric radiative transfer model, and polarimetric microwave radiometry technology.

Lalita Udpal (Life Fellow, IEEE) received the Ph.D. degree in electrical engineering from Colorado State University, Fort Collins, CO, USA, in 1986.

She is currently a University Distinguished Professor with the Department of Electrical and Computer Engineering, Michigan State University, East Lansing, MI, USA, where she is involved in the nondestructive evaluation (NDE), signal processing, and biomedical applications. Her current research interests include NDE such as the development of computational models for electromagnetic NDE, signal and image processing, data fusion, and inverse problem solutions.

Dr. Udpal is a fellow of the American Society of Nondestructive Testing (ASNT) and the Indian Society of Nondestructive Testing.

Jianliang Qian received the Ph.D. degree from Rice University, Houston, TX, USA, in 2000.

He was an Assistant Professor of mathematics with Wichita State University, Wichita, KS, USA, from 2005 to 2007; an Assistant Professor of computational and applied mathematics (CAM) with UCLA, from 2002 to 2005, and a Post-Doctoral Fellow with the Institute for Mathematics and its Applications (IMA), University of Minnesota, Minneapolis, MN, USA, from 2000 to 2002. He is currently a Professor of mathematics with a joint appointment in Computational Mathematics, Science and Engineering (CMSE) and the Director of the Michigan Center for Industrial and Applied Mathematics, Michigan State University (MSU), East Lansing, MI, USA. His research interests are in computational microlocal analysis and fast algorithms for wave propagation as well as interdisciplinary applications in biomedical and geophysical inverse problems. Together with his collaborators, he has developed fast algorithms for eikonal equations, high-frequency wave propagation, travel time tomography, and domain inverse problems of potential fields.

Dr. Qian was awarded an Outstanding Faculty Award in recognition of outstanding contributions in scholarly research and teaching at the College of Natural Science, MSU, in 2017.

Yiming Deng (Senior Member, IEEE) received the B.S. degree in electrical engineering from Tsinghua University, Beijing, China, in 2003, and the Ph.D. degree in electrical engineering from Michigan State University, East Lansing, MI, USA, in 2009.

He is currently an Associate Professor with the Nondestructive Evaluation Laboratory, Electrical and Computer Engineering Department, College of Engineering, Michigan State University. His current research interests include electromagnetic and acoustic nondestructive evaluation, structural health monitoring for multiscale, multiresolution, and multiparameter damage diagnostics and prognostics, applied electromagnetics, acoustics, and computational modeling.

Dr. Deng is a fellow of ASNT. He is an Associate Editor of IEEE TRANSACTIONS ON RELIABILITY, IEEE TRANSACTIONS ON MAGNETICS, MATERIALS EVALUATION, and RAMS Proceedings. He serves as a Panelist and a reviewer for the National Science Foundation, U.S. Department of Energy, U.S. Department of Transportation, and NDSEG Program (U.S. DoD and ASEE).